

Laser Powder Bed Fusion of Steels for Nuclear Applications

About Argonne National Laboratory

Argonne is a U.S. Department of Energy laboratory managed by UChicago Argonne, LLC under contract DE-AC02-06CH11357. The Laboratory's main facility is outside Chicago, at 9700 South Cass Avenue, Lemont, Illinois 60439. For information about Argonne and its pioneering science and technology programs, see www.anl.gov.

DOCUMENT AVAILABILITY

Online Access: U.S. Department of Energy (DOE) reports produced after 1991 and a growing number of pre-1991 documents are available free at OSTI.GOV (<http://www.osti.gov>), a service of the US Dept. of Energy's Office of Scientific and Technical Information.

Reports not in digital format may be purchased by the public from the National Technical Information Service (NTIS):

U.S. Department of Commerce
National Technical Information Service
5301 Shawnee Rd
Alexandria, VA 22312

www.ntis.gov

Phone: (800) 553-NTIS (6847) or (703) 605-6000

Fax: (703) 605-6900

Email: orders@ntis.gov

Reports not in digital format are available to DOE and DOE contractors from the Office of Scientific and Technical Information (OSTI):

U.S. Department of Energy
Office of Scientific and Technical Information
P.O. Box 62
Oak Ridge, TN 37831-0062

www.osti.gov

Phone: (865) 576-8401

Fax: (865) 576-5728

Email: reports@osti.gov

Disclaimer

This report was prepared as an account of work sponsored by an agency of the United States Government. Neither the United States Government nor any agency thereof, nor UChicago Argonne, LLC, nor any of their employees or officers, makes any warranty, express or implied, or assumes any legal liability or responsibility for the accuracy, completeness, or usefulness of any information, apparatus, product, or process disclosed, or represents that its use would not infringe privately owned rights. Reference herein to any specific commercial product, process, or service by trade name, trademark, manufacturer, or otherwise, does not necessarily constitute or imply its endorsement, recommendation, or favoring by the United States Government or any agency thereof. The views and opinions of document authors expressed herein do not necessarily state or reflect those of the United States Government or any agency thereof, Argonne National Laboratory, or UChicago Argonne, LLC.

Laser Powder Bed Fusion of Steels for Nuclear Applications

Prepared by

Srinivas Aditya Mantri
Xuan Zhang
Wei-Ying Chen

Argonne National Laboratory

August 2024

Abstract

This report provides an update on laser powder bed fusion of steels for nuclear applications. This report is a Milestone 3 deliverable in FY2024, under work package CT-24AN130401 to support research and qualification activities supported by the Advanced Materials and Manufacturing Technologies (AMMT) program here at Argonne National Laboratory (ANL). Continuing from FY23, the focus of FY24 for ANL includes further optimization of process parameters for three alloys: A709, G91, G92. The work package also includes fabricating test samples to conduct a thorough microstructural analysis and perform preliminary mechanical testing. For the same, we have used CALPHAD-based thermodynamic-kinetic modeling to optimize the experimental activities. The major outcomes of the work package are listed below.

- Following the work done in FY23, optimized process parameters were used to build larger blocks of three selected alloys: A709, G91, G92.
- Microstructural evolution of the austenitic stainless-steel alloy A709 was done after subjecting it to a series of heat treatments. The effect of different solution annealing temperatures on the microstructure and subsequently on the mechanical behavior was studied. The role of precipitation hardening treatment was also studied, with and without the role of solution annealing. Mechanical testing was done at room and elevated temperatures.
- A preliminary study was also conducted on the two ferritic martensitic alloys, G91 and G92. Microstructural evolution during the various heat treatments and their influence on the mechanical behavior was done. In some cases, the additively manufactured samples showed comparable or even better performance than their wrought counterparts.
- Future work will include further characterization of these alloys to better understand the microstructural evolution during the 3d printing process.

Table of Contents

Abstract	i
Table of Contents	ii
List of Tables	iii
List of Figures	iv
Introduction	1
Literature Review	2
2.1 Introduction	2
2.2 Austenitic Stainless Steels	2
2.3 Ferritic/Martensitic Steels.....	2
Experimental Details	4
3.1 Fabrication Technique	4
3.2 Characterization Techniques.....	4
3.3 Mechanical Testing.....	5
Results and Discussions	6
4.1 Austenitic Stainless Steel : A709	6
4.2 Ferritic/Martensitic Steel: G91	20
4.3 Ferritic/Martensitic Steel: G92	25
Conclusions and Future Work	27
5.1 Conclusions	27
5.2 Future Work	28
Acknowledgements	29
Chapter 7: References	30

List of Tables

Table 1: Optimized Process Parameters used for A709 alloy	4
Table 2: Optimized Process Parameters used for G91 and G92 alloys.....	4
Table 3: Chemical composition of Austenitic Stainless-Steel alloys in wt.%	5
Table 4: Chemical composition of Ferritic/martensitic alloys in wt.%	5

List of Figures

Figure 1: Microstructure of the as-deposited alloy A709	7
Figure 2: Microstructure of the alloy A709 after solution annealing at 1150°C/1H.....	8
Figure 3: EBSD IPF maps of alloy A709 along and across the build direction after different solution annealing times	9
Figure 4: Microstructure of the alloy A-709 after solution annealing at 1200°C/2H	10
Figure 5: Mechanical behavior of alloy A709 after solution annealing, tested at room and elevated temperatures.....	11
Figure 6: SEM images and EDS of microstructure of the alloy A-709 after precipitation treatment at 775°C/10H.....	12
Figure 7: TEM images and EDS of microstructure of the alloy A709 after precipitation treatment at 775°C/10H.....	13
Figure 8 TEM of microstructure of the alloy A-709 after precipitation treatment at 775°C/10H	14
Figure 9: SEM images and EDS of microstructure of the alloy A709 after 1150°C/1H + 775°C/10H	14
Figure 10: TEM images and EDS of microstructure of the alloy A709 after 1150°C/1H + 775°C/10H.....	16
Figure 11: SEM images and EDS of microstructure of the wrought alloy A-709 after 1150°C/1H + 775°C/10H.....	17
Figure 12: Room temperature mechanical behavior of additively manufactured A709 after precipitation treatment	18
Figure 13: Elevated temperature mechanical behavior of additively manufactured A709 after precipitation treatment	19
Figure 14:SEM Microstructure of the as-deposited alloy G91	20
Figure 15: TEM Microstructure of the as-deposited alloy G91	21
Figure 16: SEM microstructures of additively manufactured G91 after different heat treatments	22
Figure 17: EBSD IPF maps of alloy G91 along and across the build direction after different heat treatments.....	23

Figure 18: Room temperature mechanical behavior of additively manufactured G91 after different heat treatments 24

Figure 19: SEM of G92 alloy after heat treatments 25

Figure 20: Room temperature mechanical behavior of the alloy G92 after different heat treatments 26

Introduction

Additive Manufacturing is a process of fabricating objects via a layer-by-layer deposition from a 3d geometry model into complex near net shape components, thus reducing the need for post process machining, welding, and brazing[1]. Recently, there has been a huge push to explore the feasibility of using additive manufacturing techniques for the fabrication of components in energy industries[2][3]. Of particular interest for the current project, based on the AMMT roadmap, is the incorporation of current reactor materials[4]. Last year, FY2023, four US national labs, ANL, INL, ORNL, and PNNL worked on selecting current reactor materials that have a potential to benefit from additive manufacturing[5]. Following the down-selection from last year, three alloys were acquired to check the feasibility in terms of larger-scale printing, microstructural study, and its subsequent influence on the mechanical behavior. These three alloys are the austenitic stainless steel : A709, and ferritic/martensitic steels : Grade 91 and Grade 92 (henceforth referred to as G91 and G92 respectively). The current report summarizes the initial findings of microstructural evolution and mechanical behavior of these three alloys subject to various heat treatments.

Chapter 2 will provide a literature review of LPBF techniques and a more in-depth review of the alloys downselected. Following this, chapter 3 discusses the experimental details relevant to the present work, including information about the fabrication techniques, characterization techniques, and mechanical testing information.

In the next 3 chapters, there will be discussion of the current results for alloys A709, G91, and G92, followed by conclusions, and finally future work that needs to be performed.

Literature Review

2.1 Introduction

As mentioned in the previous section, based on the work in FY2023, ANL focuses on two main classes of steels as part of the current work package: (i) Austenitic Stainless Steels, (ii) Ferritic/Martensitic steels. The following section gives a brief overview of the alloys considered.

2.2 Austenitic Stainless Steels

2.2.1 A709(NF709)

First developed by the British in 1950s, the 20Cr25Ni/Nb stainless steel has been used as a fuel cladding material for the British Advanced Gas-cooled Reactor (AGR) fleet since 1962[6]. Approximately 90,000 fuel pins were present in each AGR plant, and there were 14 plants constructed and operated. While the creep strength of 20Cr25Ni/Nb was relatively low, it was sufficient for its intended application. Based on this, in the 1980s, the Nippon Steel Corporation modified the base chemical composition by adding B, Mo, and Ti to 20Cr25Ni/Nb in order to strengthen the creep resistance for ultra-supercritical boilers. The resulting austenitic stainless steel was trademarked NF 709[7]. The design criteria for developing the composition of NF 709 were to have a stable austenite devoid of the sigma and other intermetallic phases under long-term elevated-temperature service conditions, and creep-strengthened by carbonitride M(CN) precipitated in a stable, fine dispersion. Through a DOE-NE ART material down-selection and intermediate term testing program, Alloy 709, an advanced austenitic stainless-steel alloy, was recommended as a Class A structural material for the SFR because of its overall superior structural strength advantage[8][9]. While extensive work has been performed on A709 in the wrought form to have it code-qualified, there is no available literature on the additive manufacturing aspect.

2.3 Ferritic/Martensitic Steels

2.3.2 Grade 91

G91 steel was developed as a 2nd generation creep resistant alloy. ORNL modified the composition by adding small amounts of V and Nb to 9Cr–1Mo to form fine carbo-nitrides[10]. Broadly used in fossil and nuclear power plants in components operating at temperatures up to ~650°C, it is the current “workhorse” alloy and the only alloy being studied in the current work package which is included in ASME Boiler and Pressure Vessel (B&PV) Code Section III Division 5[11]. Having a Cr concentration of 9 wt. % gives very good creep strength while having a minimal increase in

the DBTT. Significant work has been performed recently on the additive manufacturing of G91 steel. Blown powder technique, wire DED, and LPBF based techniques have all been used to fabricate this alloy to understand the microstructural evolution, mechanical behavior, corrosion, and in some cases even irradiation behavior[12], [13], [14], [15]. In the case of LPBF sample, as-deposited additively manufactured G91 steel had a microstructure of lower bainitic regions surrounded by martensite. The as-deposited additively manufactured material had excellent tensile mechanical properties with greater strength than the wrought material at room and elevated temperatures, showing excellent promise for nuclear applications. Retention of strength at 300 and 600 °C for the as-deposited additively manufactured material was attributed to transitional carbides in the lower bainitic regions[16], [17].

2.3.3 Grade 92

To improve the creep properties of 2nd generation G91 alloy, G92 steel was developed as a 3rd generation creep-resistant F/M steel with the addition of tungsten and minute amounts of boron. While it has been reported to have better creep properties relative to G91, it has not been code qualified[10], [18]. In practice, the microstructure is made up of tempered martensitic lath structure which is stabilized by Cr rich $M_{23}C_6$ carbide, intra-lath MX type of Nb and V carbonitrides, martensite phase transformation induced high dislocation density, and solid solution strengthening from tungsten[19], [20]. The presence of tungsten in the $M_{23}C_6$ precipitate decreases growth rate of the precipitate during creep exposure, which in turn increases the stability of the martensitic lath structure of the steel on creep exposure[10]. Currently, there is no available research on the additive manufacturing of G92 steel.

Experimental Details

3.1 Fabrication Technique

A Renishaw AM400 LPBF machine equipped with a reduced build volume was used to fabricate all the samples. The machine is equipped with a Yb-Fiber pulsed laser with a maximum power of 400W and a beam diameter of 70 microns. Optimized parameters, provided by Renishaw, were used to fabricate two blocks, 40mm*40mm*10mm in size. This was the case for all the three alloys. The process parameters for A709 and G91/G92 are shown in Tables 1 and 2 respectively. The powders were manufactured by the company Atlantic Equipment Engineers (AEE) using argon gas atomization in 15-20 kg batches.

Table 1: Optimized Process Parameters used for A709 alloy

Scan Strategy	Laser Power (W)	Point Distance (μm)	Exposure Time (μs)	Hatch Spacing (μm)	Rotation Angle (deg)	Layer Thickness (μm)
Meander	195	60	80	110	67	50

Table 2: Optimized Process Parameters used for G91 and G92 alloys

Scan Strategy	Laser Power (W)	Point Distance (μm)	Exposure Time (μs)	Hatch Spacing (μm)	Rotation Angle (deg)	Layer Thickness (μm)
Meander	270	50	80	110	67	50

3.2 Characterization Techniques

Once the samples were printed, they were sectioned along the build direction to study the microstructure. Standard metallography techniques were employed to polish the samples for optical and electron microscopes. Samples were polished to 4000 grit SiC abrasive paper, followed by diamond suspension (3 μm and 1 μm), and by a 0.05 μm colloidal silica suspension final polish in a Buehler Vibromet. A JEOL 7500 SEM was used for electron microscopy, EBSD, and EDS. Scanning transmission electron microscopy (STEM) in high-angle annular dark field (HAADF) and bright field (BF) imaging modes were performed with a FEI Talos F200X TEM/STEM at the Center for Nanoscale Materials (CNM) in ANL to study the microstructures of selected specimens. Specimens were mechanically polished down to 100 μm in thickness, and 3 mm TEM disks were

punched out. The disks were then jet-polished until electron transparent with an electrolyte of 5% perchloric acid and 95% methanol at $-30\text{ }^{\circ}\text{C}$ with a Struers TenuPol-5 jet polisher. EDS was used to map the chemical composition of selected areas of interest. The EDS intensity maps were converted to Quantitative Hyperspectral X-ray Maps (Q-maps) for analysis.

3.3 Mechanical Testing

Dog-bone shaped tensile samples were also extracted from the two blocks, both perpendicular and parallel to the build direction. The tensile samples were SS-3 type with gage length of 7.62mm, gage width and thickness of 1.52mm and 0.76 mm respectively. Tensile tests were performed on an Instron Model 5980 Materials Testing Systems with the Instron Bluehill 3 testing software for control and data acquisition. The tester is equipped with a 3-zone furnace for air testing up to 1100°C . To begin a test, a specimen was installed into a grip that was designed for shoulder loading. The tips of two thermal couples were placed in close vicinity to the top and bottom region of the gauge section of the specimen to reflect the actual temperature of the specimen and to serve as the input of the furnace control. The temperature was brought up to the target gradually and a soaking period of 1 hour was applied to ensure a thermal equilibrium of the loading train. All tests were conducted with a strain rate of 0.001/s until rupture. Tensile tests were conducted at 25°C , 550°C , 650°C , and 750°C .

The final compositions of the powder obtained from the company Atlantic Equipment Engineers is listed below.

Table 3: Chemical composition of Austenitic Stainless-Steel alloys in wt.%

Alloy	Fe	Cr	Ni	Mn	Mo	C	N	Si	Ti	Nb	Al
A709	Bal.	20	25.4	0.91	1.51	0.06	0.16	0.44	0.04	0.26	n/a

Table 4: Chemical composition of Ferritic/martensitic alloys in wt.%

Alloy	Fe	Cr	Mo	Mn	W	V	Nb	C	Ni	Si	N
G 91	Bal.	8.3	0.9	0.43	n/a	0.2	0.06	0.1	0.17	0.42	n/a
G 92	Bal.	8.7	0.5	0.45	1.9	0.2	0.07	0.09	n/a	0.14	n/a

Results and Discussions

The results from each alloy will be presented following the same structure. The microstructure of the as-deposited sample will be shown in detail using advanced characterization techniques like scanning electron microscopy, EDS/EBSD, and transmission electron microscopy. This will be followed by the microstructure analyses of the heat-treated samples. Finally, the mechanical behavior of these alloys following room and elevated temperature tensile testing will be discussed.

4.1 Austenitic Stainless Steel : A709

4.1.1 *As Deposited*

The microstructures of the as-deposited A709 are shown in Figure 1. The BSED image features a typical microstructure observed in other as-deposited austenitic stainless steels[21], [22]. A high magnification image of one of the grains is shown in the inset. The presence of cell boundaries, another typical feature in austenitic stainless steels, is clearly present. At this scale, no presence of any precipitates is noted. The sample was further analyzed using S/TEM to ascertain the presence of any nanometer sized secondary phases. BFTEM image in (c) and (d) do not clearly reveal the presence of any secondary phases. The SADP obtained along $[001]\gamma$, shown as inset, confirms this. No superlattice spots corresponding to any secondary phases are present. The BFTEM shows a very high density of dislocations present in the system. The dislocation cells can also be clearly observed. STEM-EDS mapping reveals a slight amount of Cr segregation along the cell boundaries. Following this, based on the work by Sham et al[23], [24], the as-deposited samples were then solution annealed at 1150°C/1H.

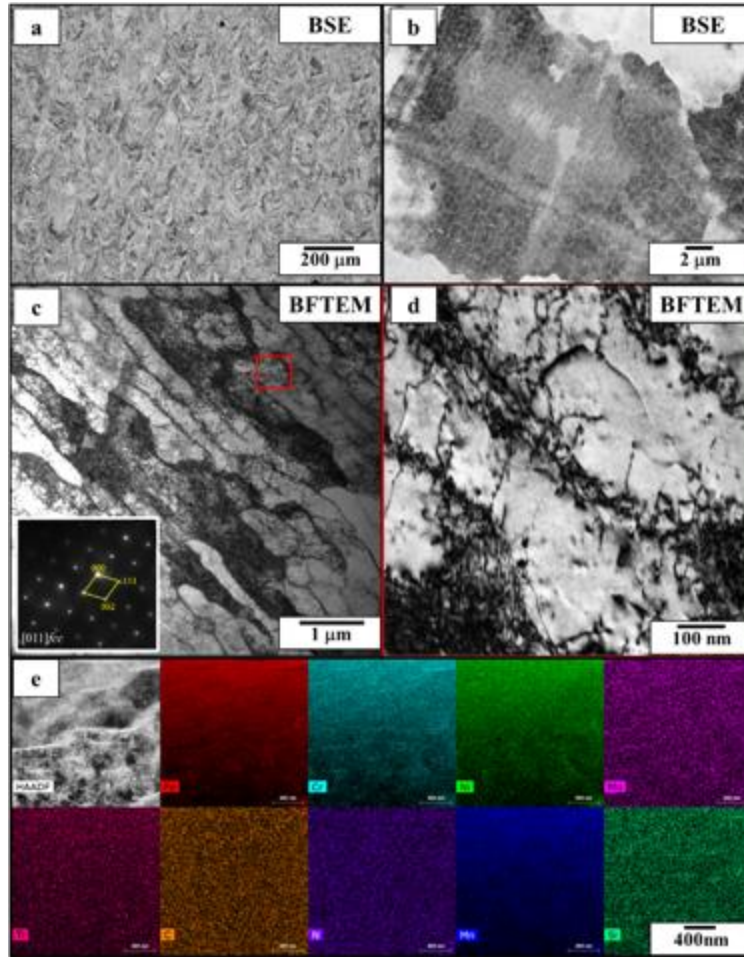


Figure 1: Microstructure of the as-deposited alloy A709

4.1.2 Effect of Solutionizing Annealing

TEM analysis was performed on solution-annealed specimen to look for nano-precipitates. Figure 2 (a-c) show a series of BFTEM images at different magnifications. The presence of secondary phases is clearly noted. Based on the SADP (inset in Figure 2c) analysis, these precipitates are determined to be MX carbonitrides, which are around 50nm in size. MX precipitates also have an FCC crystal structure and have an orientation relationship with the matrix, i.e. $[001]\gamma // [011]MX[25]$. The precipitates are mostly lined up near the dislocations and seem to be pinning them. It has been reported in literature that the dislocations act as nucleation sites for these MX precipitates[26]. The presence of these MX carbonitrides on the dislocations is known to provide good creep resistance. HAADF STEM image in Figure 2d also shows the same and the EDS maps reveal the MX carbonitrides are made of Ti, Nb (N, C). Considering that this heat treatment was chosen based on previous work done on wrought materials, it is of interest to see if the same heat

treatment would work for additively manufactured materials. Interestingly though, a high number of dislocations are still present which indicates the heat treatment was not totally effective. As such, the as-deposited samples were further heated at 1200°C for 1H and 2H.

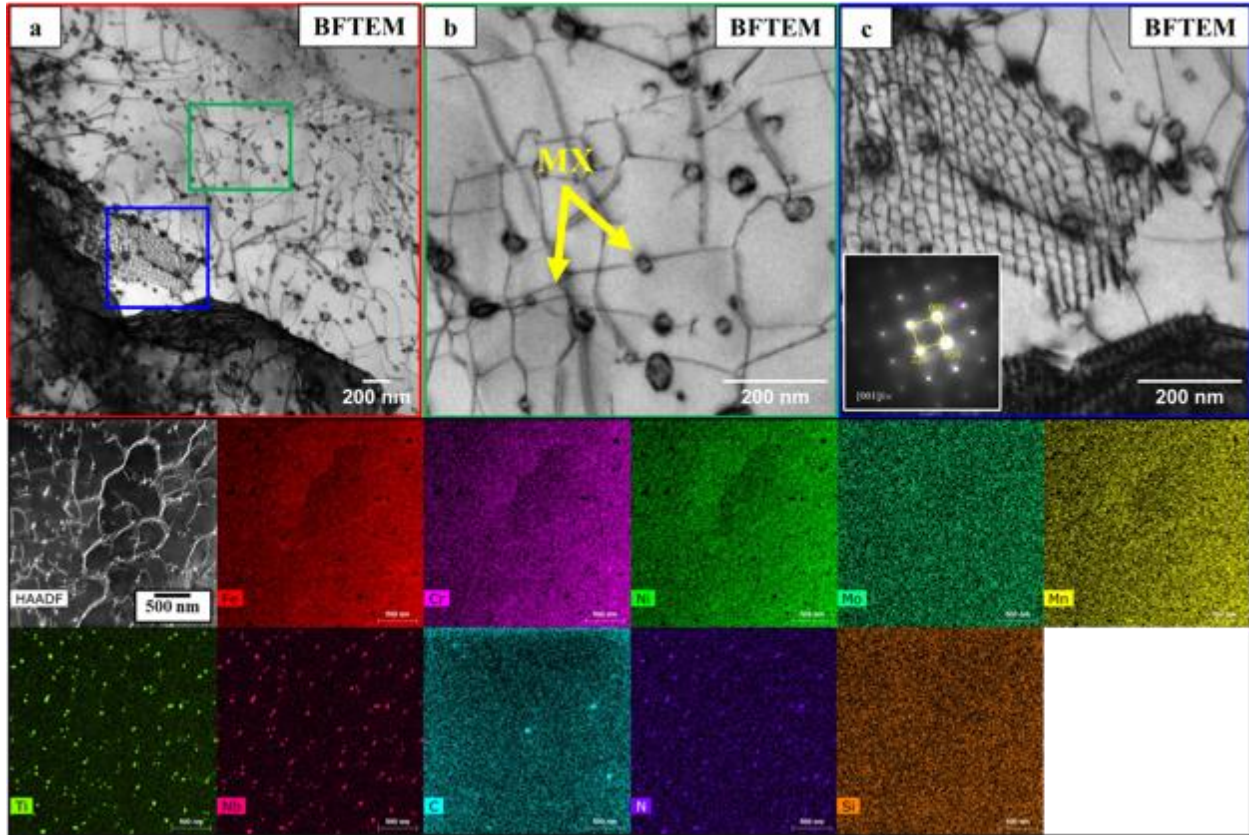


Figure 2: Microstructure of the alloy A709 after solution annealing at 1150°C/1H

Figure 3 shows the EBSD IPF maps of all 4 conditions, both across and along the build directions. In the as-deposited condition, slightly elongated “U-shaped” grains were observed along the build direction with sizes ranging from 10 μm microns to 120 μm with an average grain size of 40 microns. The “checkerboard” pattern noticed in the IPF maps perpendicular to the build direction is due to the scanning pattern employed during the deposition process. The grains are about ~ 30 microns in size. Annealing this sample at 1150°C/1H did not seem to influence either the grain morphology or size in both vertical and horizontal samples. The grain sizes from the EBSD analysis parallel and perpendicular to the build direction were noted to be ~ 40 and ~ 30 microns respectively. Finally, the samples which were annealed at 1200°C start to show a difference. After 2H, the grain size slightly increased in both the samples. In the vertical sample, the grains start to lose the “U” shape and go up to 50 microns in size. Similar change in the grain morphology was

noted in the horizontal sample, breaking down the checkerboard pattern. A few annealing twins also start to form in this sample and have been highlighted in the Figure. This shows that the samples are still only partially recrystallized, and possibly longer annealing times might be required to fully recrystallize the samples [27].

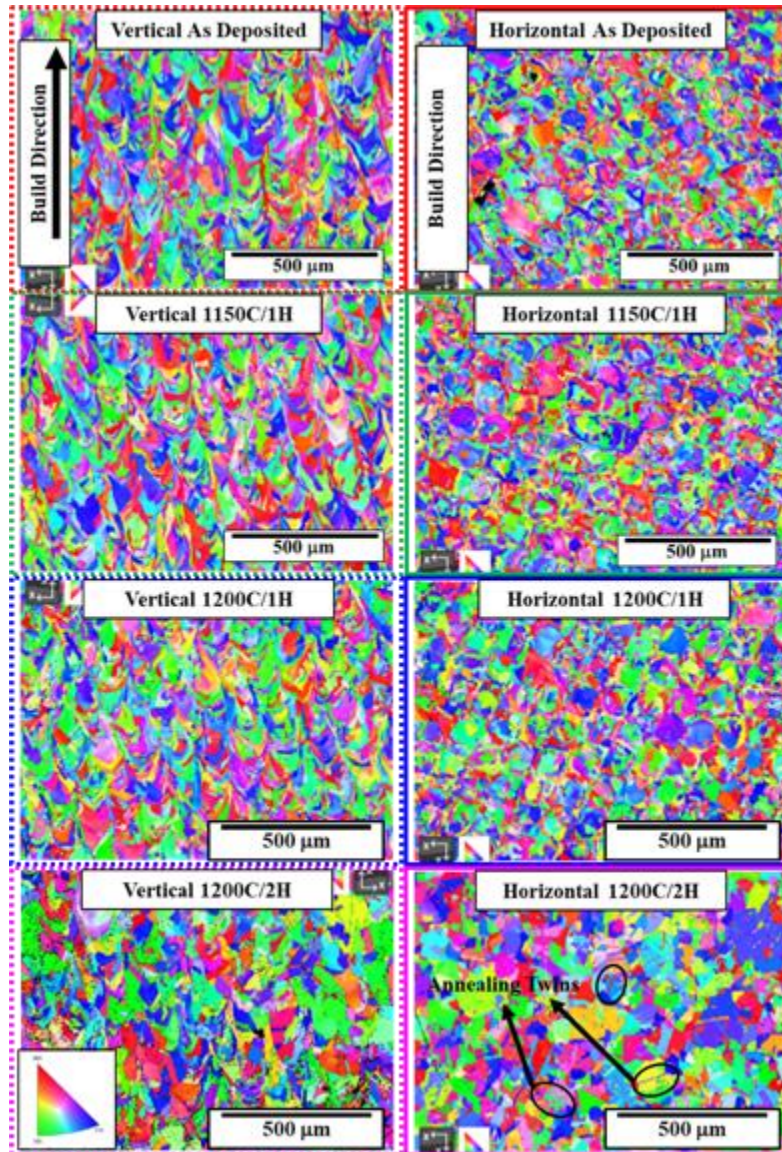


Figure 3: EBSD IPF maps of alloy A709 along and across the build direction after different solution annealing times

While the EBSD maps did reveal some information regarding the recrystallization, it does not provide the full picture in terms of dislocations and/or nano-precipitates within the γ -matrix. Annealing the sample at 1200°C/2H did not significantly modify the microstructure compared to the 1150°C/1H sample. The BFTEM images in Figure 4, at different magnifications, reveal the

presence of MX-carbonitrides in the γ -matrix. The overall size of these MX precipitates seems to be slightly larger than the ones noticed in 1150°C/1H with some of the precipitates being as large as 100nm. In the specific areas captured in this micrograph, the overall number also seems to be higher. Another interesting thing of note to be observed in these micrographs is the presence of what appears to be “fishnet” type of dislocations. These dislocations seem to be trapping the precipitates within them, which during deformation, could enhance the overall mechanical properties. This also shows that annealing the sample at 1200°C/2H also does not completely get rid of the dislocations within the system. HAADF-STEM EDS maps confirm that these are indeed MX precipitates, being rich in Ti, Nb (N, C).

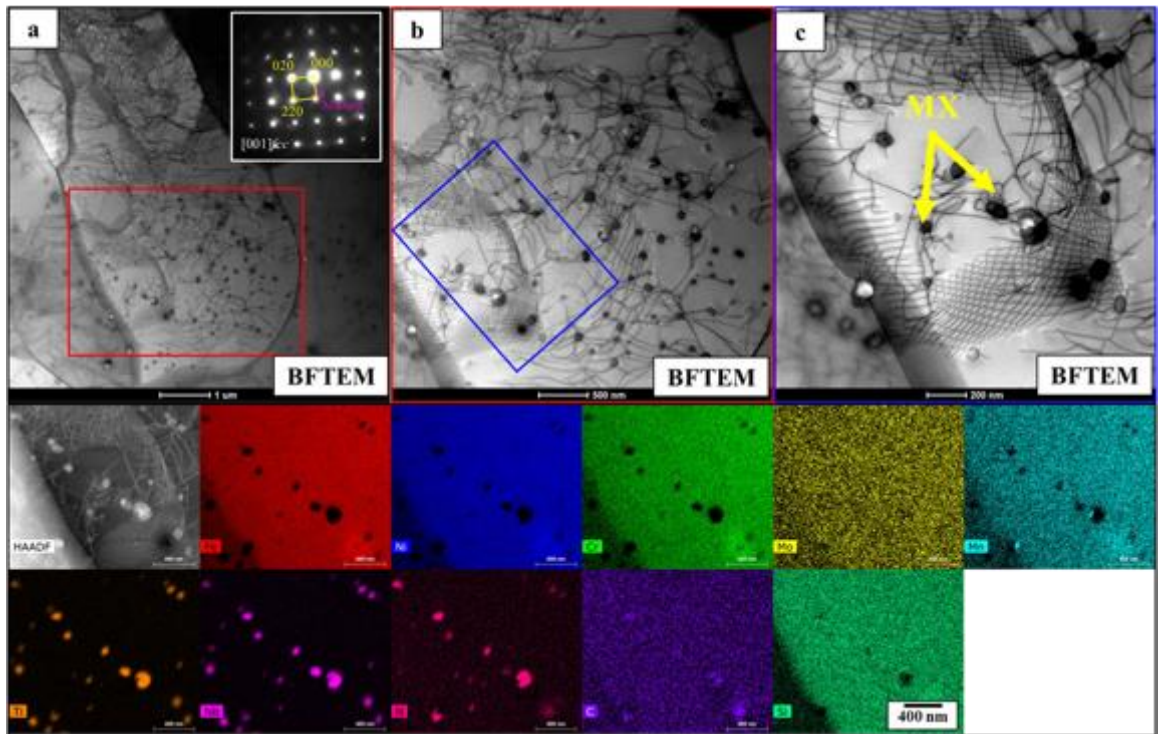


Figure 4: Microstructure of the alloy A-709 after solution annealing at 1200°C/2H

Mechanical Testing

Following the microstructural analysis, to understand the effect of these aforementioned heat treatments on the mechanical behavior, room and elevated temperature tensile tests were performed on the samples, both along and across the build direction. The mechanical behavior of these samples is summarized in Figure 5. Figure 5a shows the engineering stress vs strain plot for the samples tested at room temperature. All the samples tested across the build direction show a

greater yield and ultimate tensile strength compared to samples tested along the build direction. The as-deposited samples showed the highest strength with yield strength around ~665MPa and UTS of ~790MPa. Though the as-deposited samples had the highest strengths, their ductilities were lower compared to the aged samples. With an increase in the aging time, the strengths decreased while the ductility increased. The sample aged at 1150°C/1H showed a yield strength of ~490MPa and UTS of ~710MPa while the sample aged at 1200°C/2H had a yield strength of ~300MPa with UTS reaching ~610MPa. These values are to be expected when we look at the overall microstructures of these samples. The as-deposited sample with highest number of strain/dislocations has the higher YS/UTS. With aging, along with the stress relief, there is also a change in the overall grain size which reduces the strengths. Another interesting point to note here is that aging the sample leads to an increase in the strain-hardenability of the alloy. Following the room temperature tests, the samples were also tested at 550°C, 650°C, and 750°C, and these are shown in Figure 5(b-d). As expected, with an increase in the testing temperature, the overall strength of the alloy decreases. It should be noted here that the scale bars shown here for the graphs are different.

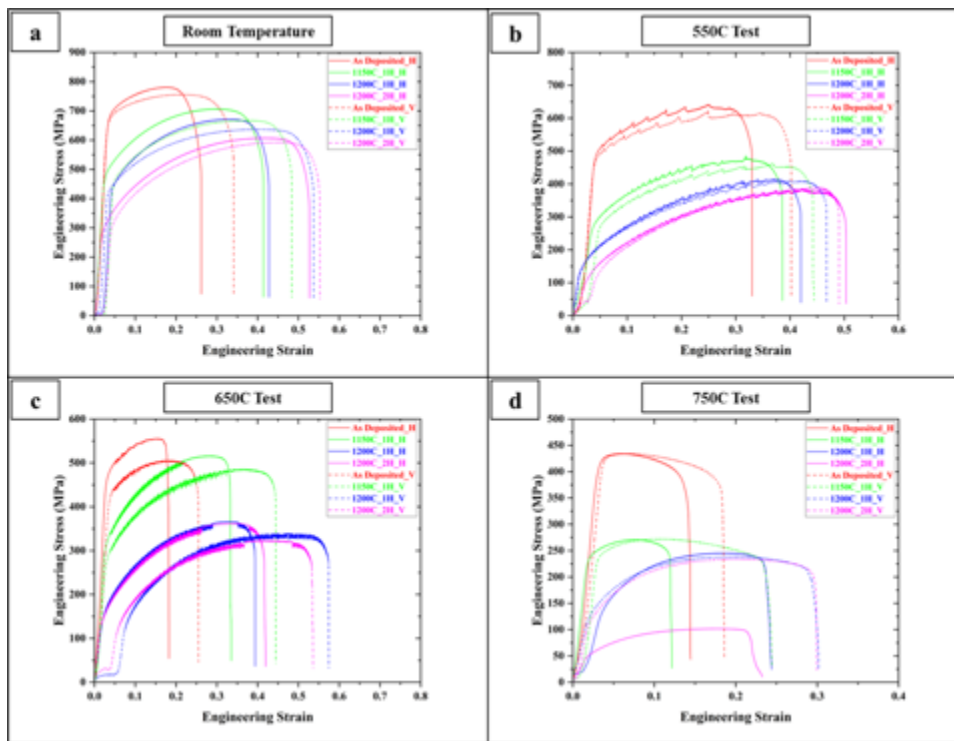


Figure 5: Mechanical behavior of alloy A709 after solution annealing, tested at room and elevated temperatures

4.1.3 Effect of Precipitation Treatment

A709 was originally developed as precipitation strengthened alloy. As such, in order to further explore this, precipitation invoking heat treatments were also done on the alloys. The samples were heated to 775°C/10H (henceforth called PT) based on the work done by Zhang et al and Sham et al [7], [9]. To understand the effect of solution annealing on the subsequent microstructure evolution, the samples which were solution annealed were also aged at 775°C/10H. The microstructure of these two conditions and their comparison with a wrought alloy undergoing the same heat treatment will be discussed next.

Figure 6 shows the sample which was given a precipitation treatment directly after deposition. A large number of precipitates can be seen in the SEM images. The presence of both grain boundary and intra-granular precipitates is noted. The EDS maps reveal that while most of the grain boundary precipitates are carbides (possibly $M_{23}C_6$), the intra-granular precipitates seem to be MX carbonitrides.

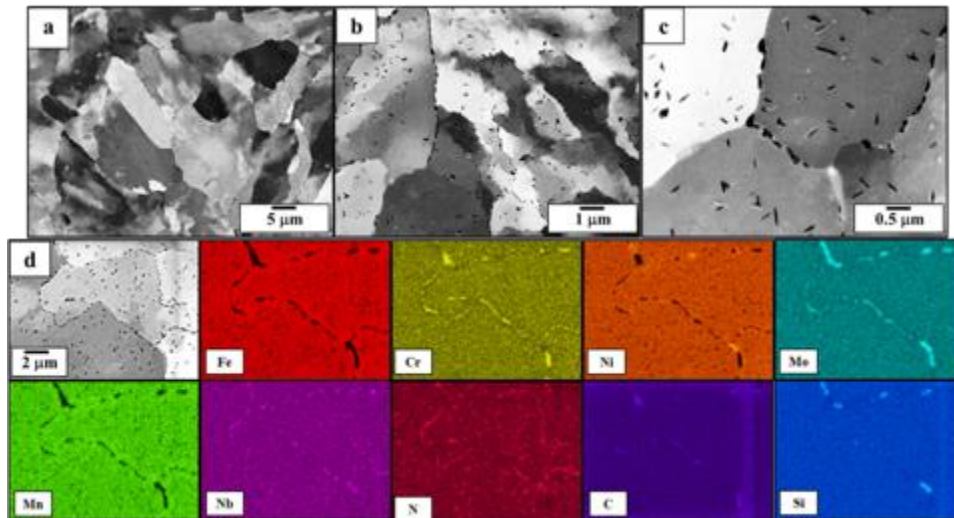


Figure 6: SEM images and EDS of microstructure of the alloy A-709 after precipitation treatment at 775°C/10H

While the presence of the precipitates is clearly noted, SEM analysis alone does not reveal their nature. As such, further TEM analysis was also performed on this condition and is shown in Figure 7. A series of BFTEM images at different magnifications show precipitates along both the grain and cell boundaries. Furthermore, there are more precipitates present within the cell boundaries, mostly along dislocation lines. The precipitates along the grain boundaries, (highlighted in Figure 7c), have a very distinct faceted shape, often associated with $M_{23}C_6$ carbides. Similar to the sample,

which was SA, dislocation lines seem to be the breeding ground for other *smaller* precipitates. Selected area diffraction analysis done along two different zone axes $[011]\gamma$ and $[001]\gamma$ shows superlattice reflections which are indicative of both $M_{23}C_6$ and MX carbonitride precipitates. The parent FCC (γ) phase and the carbides have the OR $[110]\gamma \parallel [101]M_{23}C_6$. The HAADF-STEM EDS maps of the AD + PT microstructure is shown in Figure 7d. A significant amount of precipitation is noted in this condition, both along the grain and cell boundaries. The grain boundary precipitates clearly show segregation of Cr, Mo, Mn, and C, further confirming these to be $M_{23}C_6$ precipitates. The presence of some of these carbides within the grain interiors, in plate shape, is also noted here. While the grain boundaries are adorned with the carbides, the cell boundaries are fully coated with Ti, Nb, and N. The high-volume fraction of these precipitates is expected to play a key role in the overall mechanical behavior of the alloy A709.

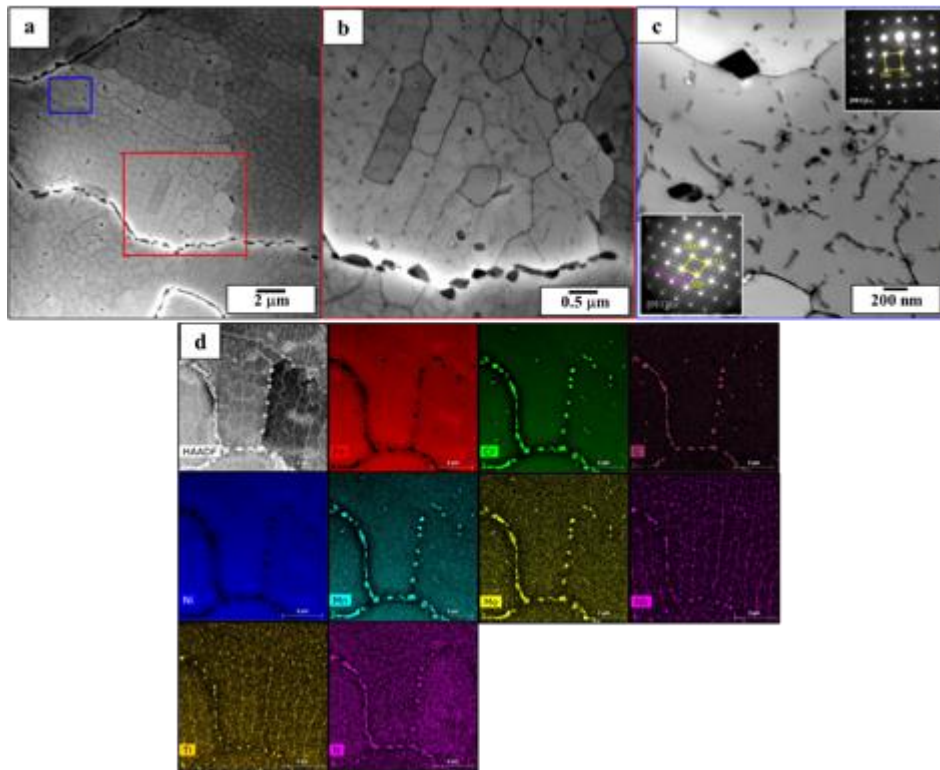


Figure 7: TEM images and EDS of microstructure of the alloy A709 after precipitation treatment at 775°C/10H

It should also be noted here that the annealing of the sample at 775°C/10H did not result in stress relief. A high number of dislocations are still present and can be seen in Figure 8.

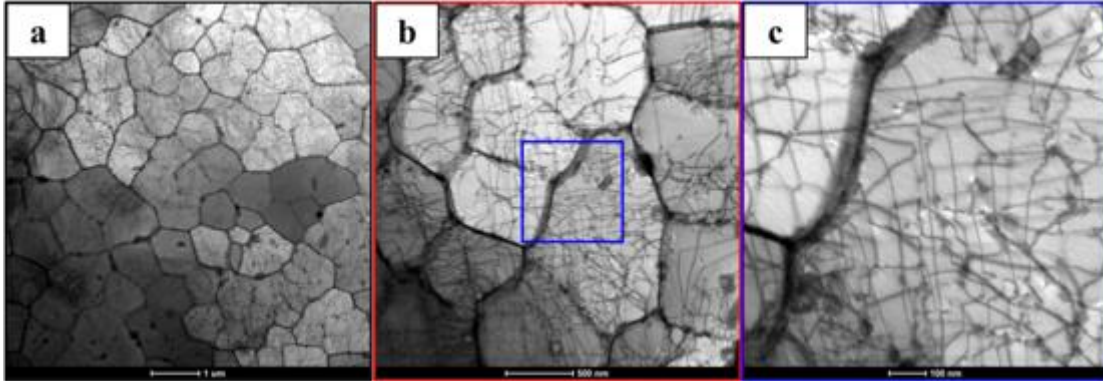


Figure 8 TEM of microstructure of the alloy A-709 after precipitation treatment at 775°C/10H

Compared to the sample which was directly given a precipitation treatment at 775°C/10H, the sample which was first solution annealed at 1150°C/1H and then given precipitation treatment, shows a fewer number of precipitates on first viewing. The BSE images in Figure 9 reveal the presence of both grain boundary precipitates as well as intra-granular precipitation. Similar to the PT sample, the grain boundary precipitates seem to be $M_{23}C_6$ carbides. EDS mapping at this length scale could not clearly ascertain the nature of intra-granular precipitation.

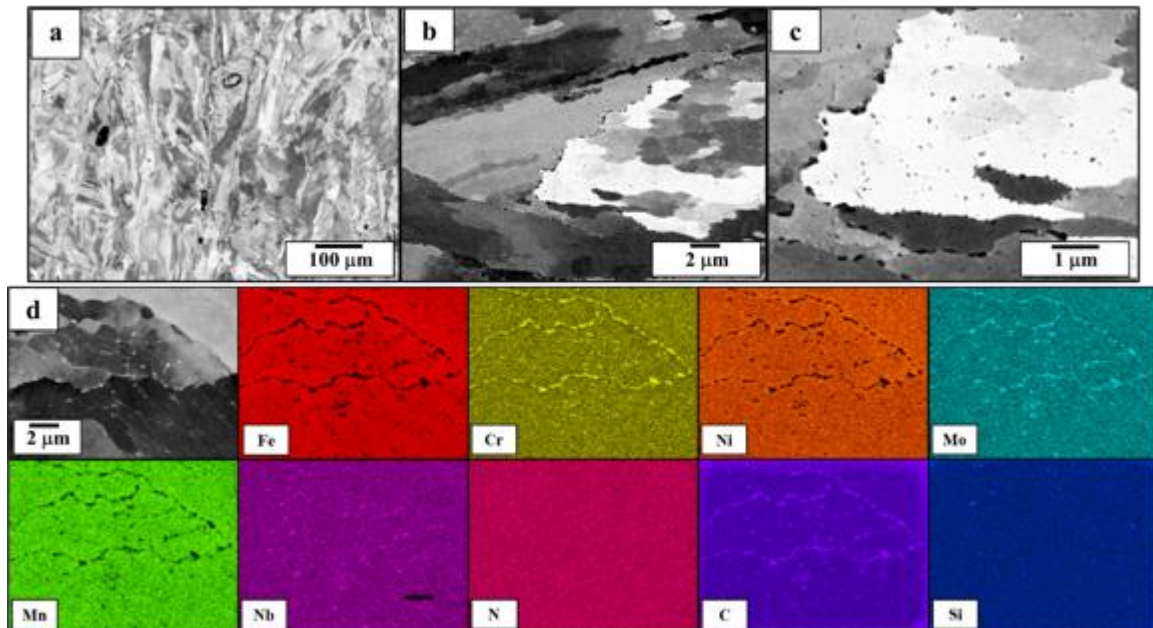


Figure 9: SEM images and EDS of microstructure of the alloy A709 after 1150°C/1H + 775°C/10H

TEM analysis of this sample is shown in Figure 10. The presence of both $M_{23}C_6$ carbides and MX type precipitation is clearly noted here. The SADP along $[001]_{\gamma}$ shows the superlattice reflections of both $M_{23}C_6$ and MX precipitates. The corresponding DFTEM images are taken from the spots highlighted in the SADP. It can be seen in Figure 10c and 10d that while the MX precipitates adorn the grain interiors, the grain boundaries are covered by the carbides. The size scale of these precipitates is very similar to the precipitate sizes noted in the PT condition. The HAADF-STEM EDS maps provide further insights. Based on the maps shown here, there seem to be three distinct precipitates: $M_{23}C_6$ carbides which are also stabilized by some amount of Mn and Mo along the grain boundaries. The presence of these inside the grains is also noted. Ti and Nb based nitrides (MX) are also present throughout the sample within the grain interiors. Interestingly, other than these two precipitates, a third precipitate can be observed growing next to one of the grain boundary carbides. This precipitate, which is rich in Ni, Si, N, and some amount of Cr is assumed to be θ phase. Previous reports have shown the presence of this precipitate in the aged sample and have theorized it to be forming from the carbides[25][26].

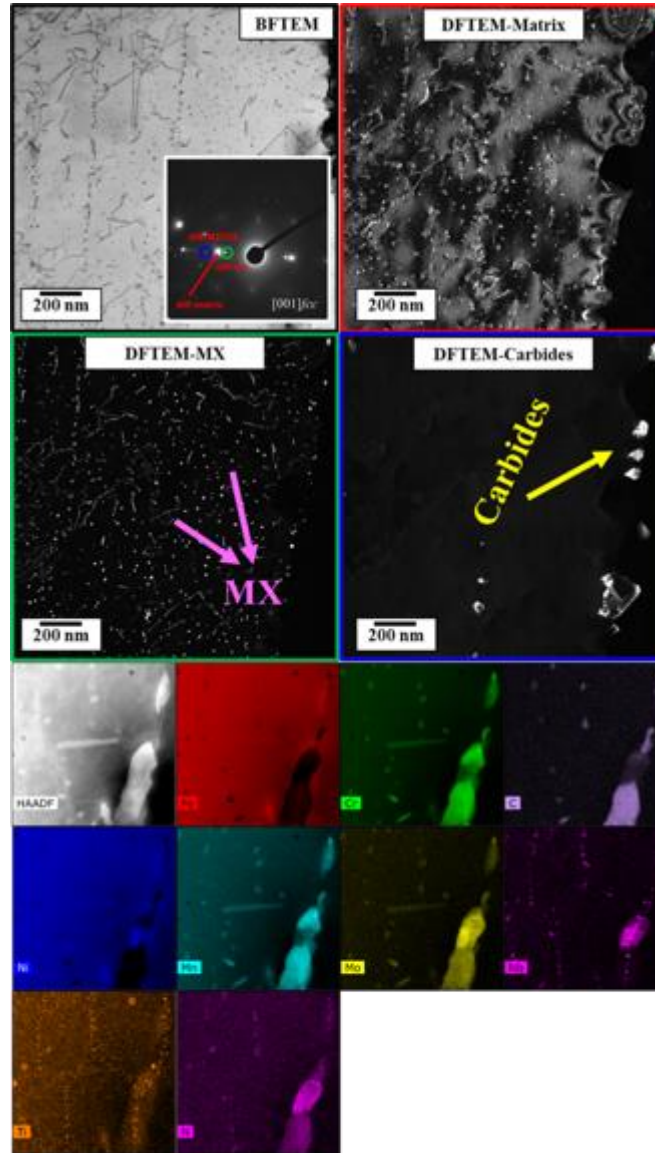


Figure 10: TEM images and EDS of microstructure of the alloy A709 after 1150°C/1H + 775°C/10H

The microstructure of the additively manufactured sample is then compared with a wrought sample to see the differences. The wrought sample was originally solution annealed at 1150°C/1H and then aged at 775°C/10H. Figure 11 shows the SEM images and EDS mapping of the same. The grain size is approximately around 110 μm with precipitates mostly present along the grain boundaries. The presence of some annealing twins is also noted in this sample and is highlighted in the Figure 11b. Based on the morphology in Figure 11c, it seems that there are different kinds of precipitates present in this condition: blocky precipitates along the grain boundaries and plate like precipitates along the grain interiors and along the twin boundaries. The grain boundary

precipitates can be clearly identified as $M_{23}C_6$ ($M = \text{Cr, Mo}$) carbides. The presence of some amount of MX precipitation is also seen.

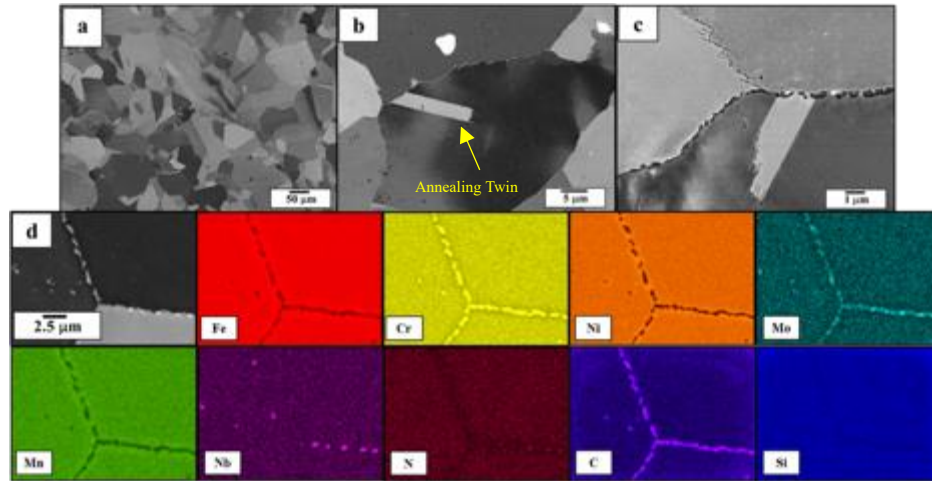


Figure 11: SEM images and EDS of microstructure of the wrought alloy A-709 after 1150°C/1H + 775°C/10H

Mechanical Testing

Room Temperature Tensile Properties

The room temperature tensile properties of the LPBF A709 stainless steel along and across the build direction are compared in Figure 12. The samples tested across the build direction exhibited slightly higher yield strength with a small decrease in the ductility. The as-deposited sample, owing to high amount of residual stresses present, exhibited a high strength in both vertical and horizontal samples with yield strength of 638 and 656 MPa respectively. Once the sample is solution annealed, there is a decrease in the overall strength accompanied by an increase in the ductility; the horizontal and vertical sample have yield strengths ~400MPa with strain to failure of >40%. Interestingly the samples which were precipitation hardened showed a big difference in the mechanical behavior, depending on whether or not a prior solution annealing was done. The AD+PT shows the highest strength among all the samples tested with a yield strength of ~680 MPa and UTS of ~850MPa. As was seen in the microstructure in the Figure 7, a high number of dislocations + the presence of precipitates ($M_{23}C_6$, MX, θ) can explain the high strength of this condition. In contrast, the sample which was aged after solution annealing had strengths comparable to the just solution annealed sample[7].

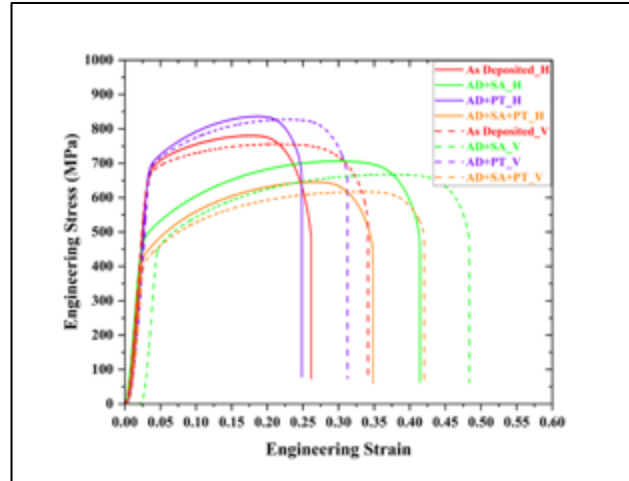


Figure 12: Room temperature mechanical behavior of additively manufactured A709 after precipitation treatment

High Temperature Tensile Properties

The samples were then tested at elevated temperature of 550°C. As expected, with an increase in the testing temperature, there is an overall decrease in the yield strength of all the conditions. In the samples tested at 550°C, all the curves exhibited serrated flow during the tensile deformation. Generally, the occurrence of serrated flow has been attributed to the dynamic strain aging (DSA) effect. DSA is caused by the pinning and unpinning of dislocations and solute atoms. In the case of the samples which are deformed at 550°C, it is likely that the diffusion of substitutional solutes causes DSA. As such it is interesting to notice the change in the “amplitude” and “frequency” of the serrations in the stress-strain curves. The AD sample shows the largest frequency. It should be remembered that the AD sample has no precipitation within the matrix and has the highest amount of segregation of substitution solutes. By aging the sample, we can see that different precipitates are formed in the matrix. For the samples which undergo precipitation treatment, either direct or indirect, a large number of carbides and MX are present in the matrix. The formation of such precipitates will lead to a reduction in solute content within the matrix and thus lower the chances of their interaction with the dislocations. This causes the change in the serrated nature of the curves. The samples with highest number of precipitates show the smallest frequency and amplitude.

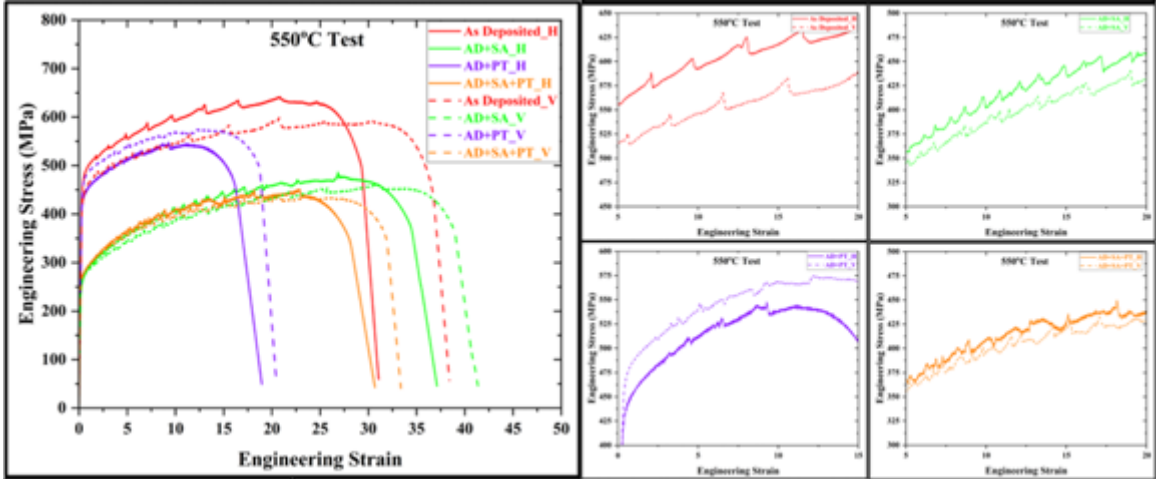


Figure 13: Elevated temperature mechanical behavior of additively manufactured A709 after precipitation treatment

4.2 Ferritic/Martensitic Steel: G91

Similar to the A709 alloy, the microstructure of the as-deposited sample was investigated first using advanced characterization techniques.

4.2.1 As Deposited

Figure 14 shows the microstructure of the sample along the build direction. The presence of “u-shaped” grains seems to be a common feature among the additively manufactured steels. The higher magnified image in Figure 14b is rotated 90° to give a better understanding of the microstructural features. Here, two distinct features can be clearly noted, and these are then further magnified and shown in Figure 14c and d. The magnified area in green shows the presence of small lath-like precipitates within the *bcc* matrix. On the other hand, the area magnified in the blue box shows what seems to be martensite like features. Interestingly, both these features can be delineated based on the melt pool of the laser. Further studies are in progress to fully understand this microstructure evolution.

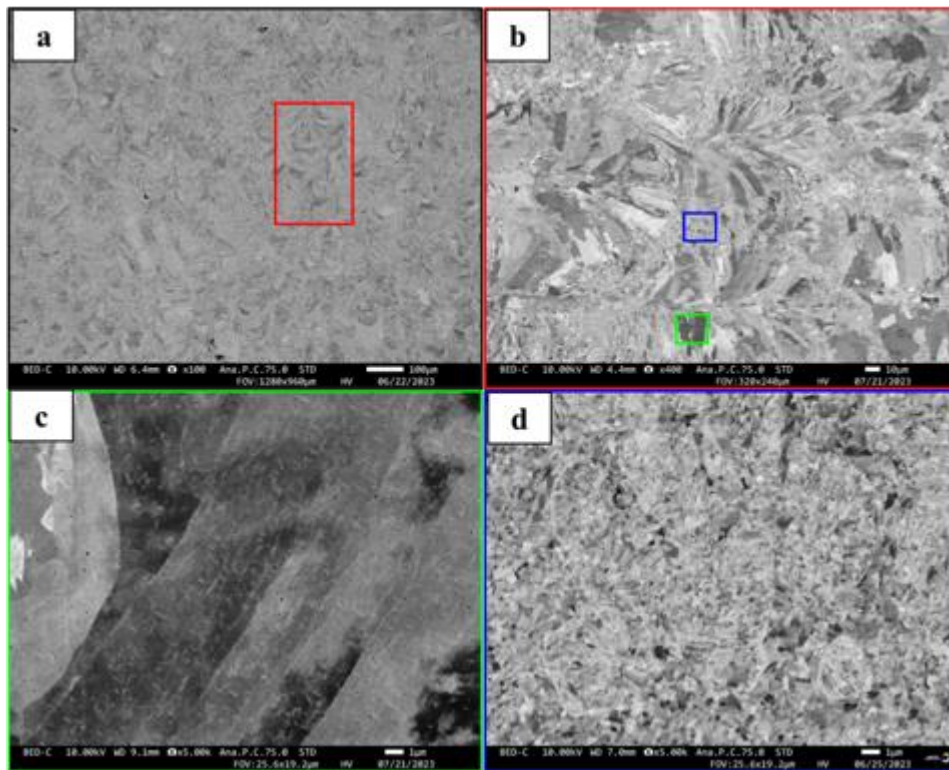


Figure 14: SEM Microstructure of the as-deposited alloy G91

Following the SEM analysis, a 3mm disc was made to look at the finer features in a transmission electron microscope. Figure 15 shows the presence of two different kinds of precipitates within

the matrix. It should be noted here that the image is from an area similar to the green box shown in Figure 14. Based on literature review, the lath-like features are noted to be θ phase while the larger precipitate appears to be carbide ($M_{23}C_6$). As mentioned, further studies are in progress to fully understand the microstructural evolution of G91 during additive manufacturing process.

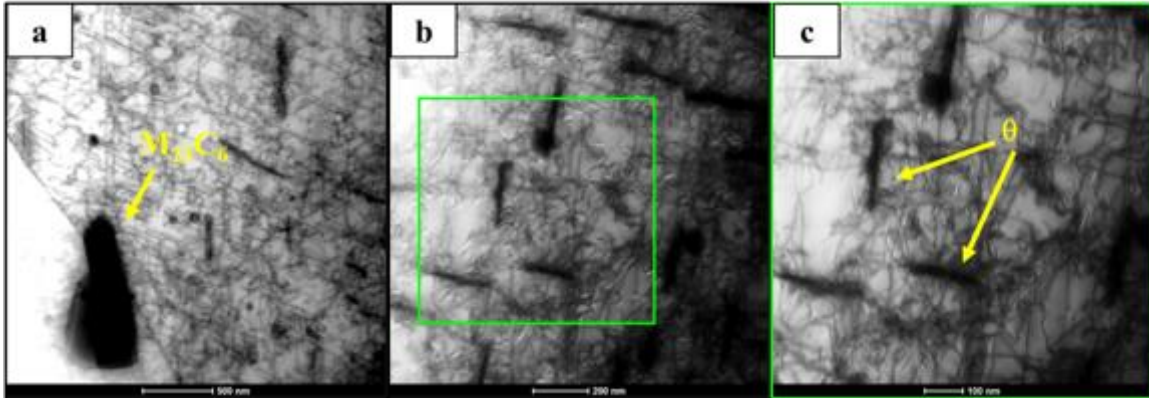


Figure 15: TEM Microstructure of the as-deposited alloy G91

4.2.2 Effect of Heat Treatments

For alloy G91 the standard heat treatments recommended are normalizing and tempering[10], [12], [17]. These two different heat treatments are performed at $1070^{\circ}\text{C}/15\text{min}$ and $770^{\circ}\text{C}/45\text{min}$ respectively. As an additional step, we have also performed another heat-treatment including both the aforementioned steps. Following normalizing the sample at $1070^{\circ}\text{C}/15\text{min}$ we tempered the sample at $770^{\circ}\text{C}/45\text{min}$. All these micrographs are put in comparison and shown in Figure 16. These micrographs are taken along the build direction. The as-deposited samples are shown in red boxes at different magnifications, $1070^{\circ}\text{C}/15\text{min}$ in green boxes, $770^{\circ}\text{C}/45\text{min}$ in turquoise, and the $1070^{\circ}\text{C}/15\text{min} + 770^{\circ}\text{C}/45\text{min}$ (two-step) in blue boxes. It should be mentioned here that all the samples were water quenched after the specified heat treatments. Due to the quenching, after holding the sample at 1070°C , the microstructure appears to be completely transformed into martensite. Martensitic laths can be clearly seen in the high magnification images. No trace of the starting microstructure was found. When the sample was tempered at 770°C , the original grain structure was retained, but the martensite phase detected along the melt-pools in the as-deposited condition seems to have reduced. The formation of newer phases along the grain boundaries is also noted. Finally, the sample which underwent both these steps seems to have a “tempered”

martensitic structure. By aging the sample at 1070°C, the original microstructure is lost and changes to martensitic phase. By annealing this sample at 770°C, tempering of this martensite takes place leading to a “softer” phase. At this scale, we did not notice the presence of any secondary precipitates.

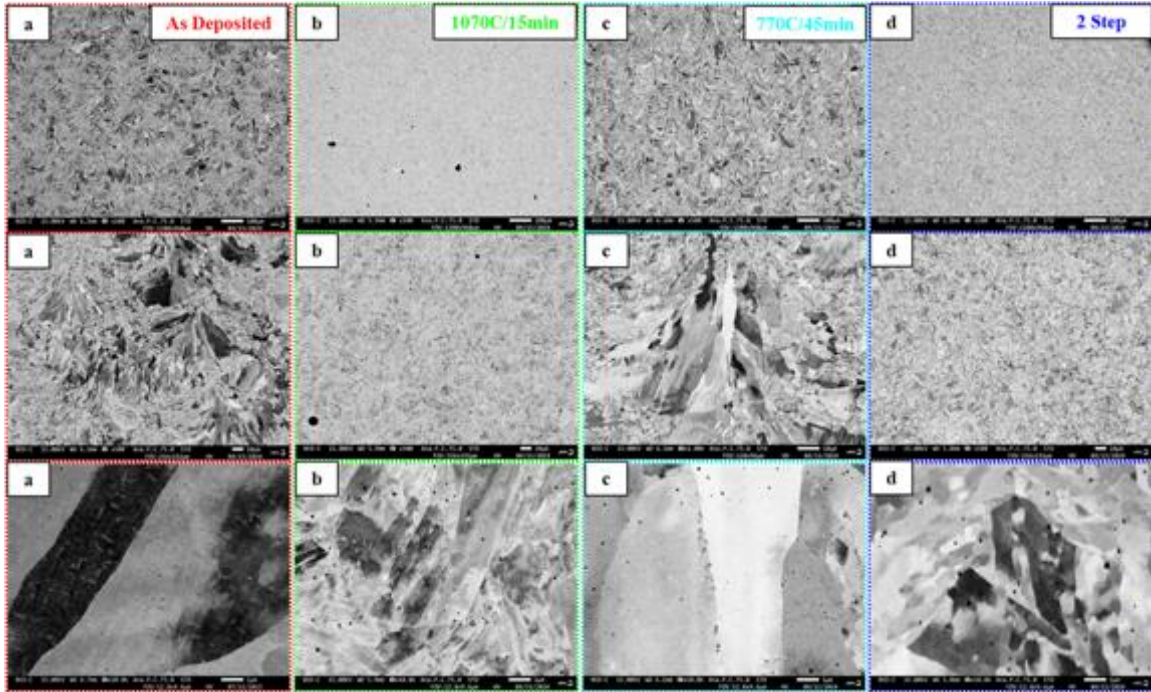


Figure 16: SEM microstructures of additively manufactured G91 after different heat treatments

Figure 17 show the EBSD IPF maps of all four conditions, both across and along the build directions. In the as-deposited condition, slightly elongated “U-shaped” grains were observed along the build direction. Finer grains were present between the larger grains. Some of the regions were not indexed and are shown as black regions. The “checkerboard” pattern noticed in the IPF maps perpendicular to the build direction is due to the scanning pattern employed during the deposition process. The grains are about ~100 microns in size and also have finer grains between the larger grains. Aging the sample at 1070°C alters the microstructure significantly. The grain sizes from the EBSD analysis were noted to be ~5 and ~10 microns along vertical and horizontal directions respectively. Aging the sample at 770°C also seemed to have an effect. Tempering of the microstructure leads to dissolution of the martensite phase and indexing was more clearly observed. The overall grain morphology looks very similar to the as-deposited conditions. Finally, the samples which underwent the two-step heat treatments were also analyzed. The EBSD IPF maps are very similar to the samples annealed at 1070°C. The heat treatment at 770°C seemed to

make no significant difference in this case. To understand the effect of these heat treatments on the mechanical behavior, room temperature tensile tests were performed on these samples and are described in the following section.

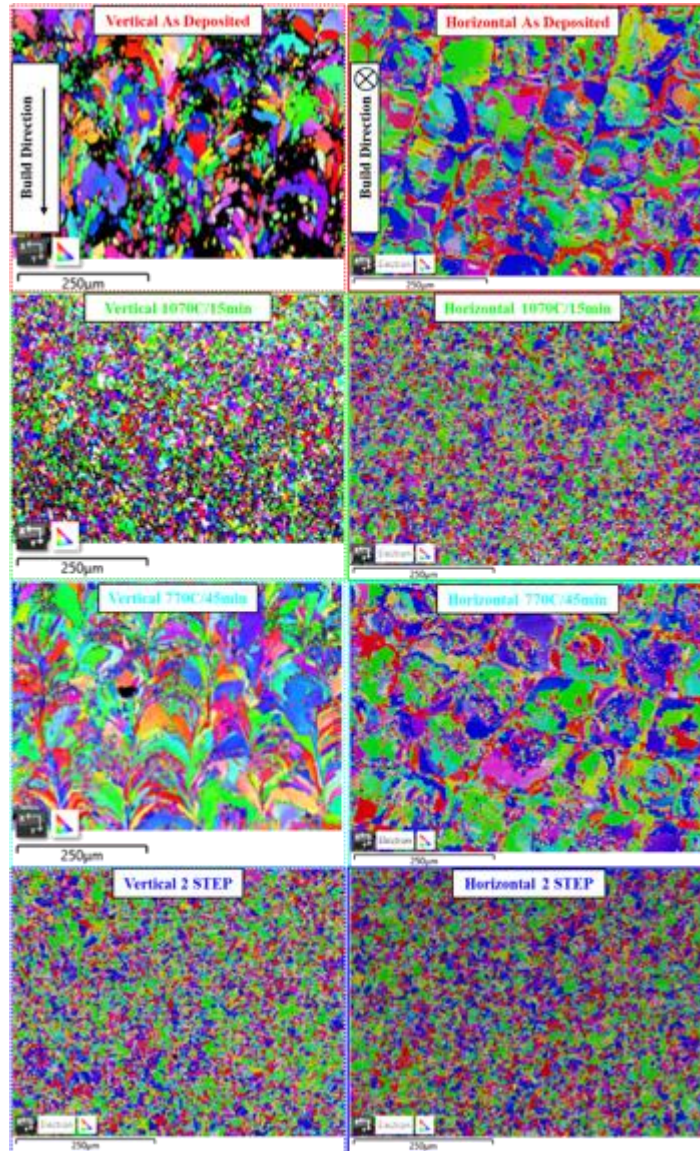


Figure 17: EBSD IPF maps of alloy G91 along and across the build direction after different heat treatments

4.2.3 Mechanical Testing

The mechanical behavior of these samples is summarized in engineering stress vs strain plot shown in Figure 18. The as-deposited samples show a good combination of strength and ductility with UTS reaching around 900MPa and strain to failure around 20%. The samples aged at 1070°C showed the highest strength with UTS around 1300MPa. This is to be expected as the

microstructure is solely made up of martensite. The samples which underwent the 770°C heat treatment, with and without the 1070°C treatment, had the lowest values of strength with values around 600MPa. Further work is being doing in order to test these samples at elevated temperatures and to study the deformation behavior.

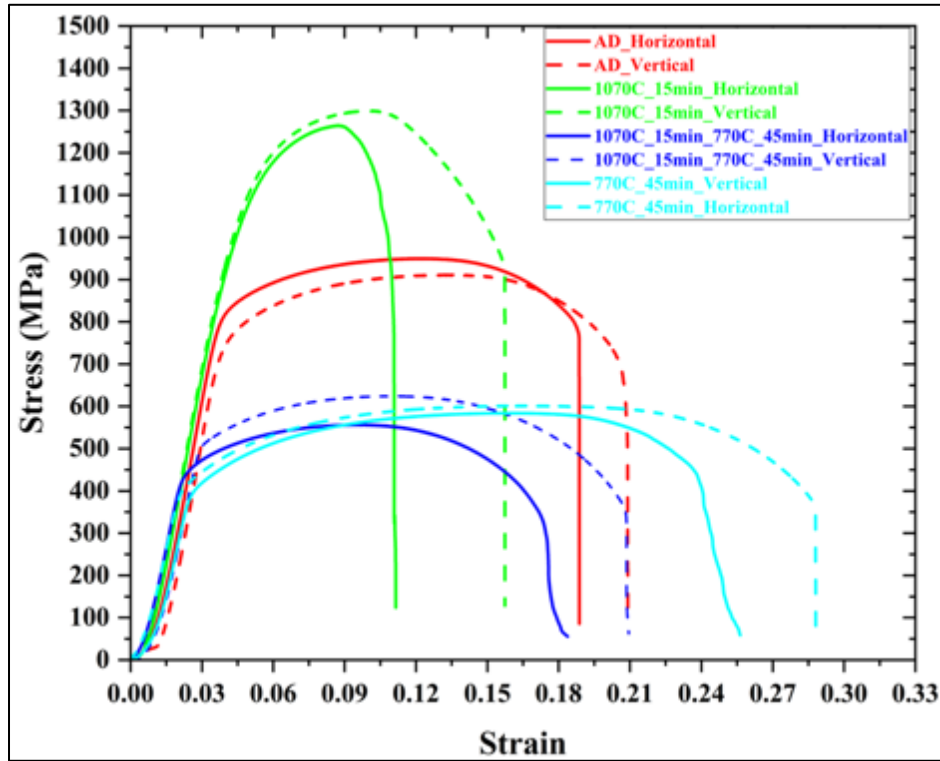


Figure 18: Room temperature mechanical behavior of additively manufactured G91 after different heat treatments

4.3 Ferritic/Martensitic Steel: G92

G92 was the last sample characterized and tested as part of the current work for FY2024. Same process parameters were used to process G92 as for G91. The major differences between the alloys are the addition of W in G92 along with a slight reduction in percentage of Mo. This leads to no significant change in the microstructural features, but has some effect on the mechanical behavior, especially due to the solid solution strengthening capabilities of W.

4.3.1 Microstructure

Similar to G91, after the deposition, the alloy was subject to three different heat treatments. These are shown in Figure 19 at different magnifications. The as-deposited sample has a mixture of bcc phase along with some secondary precipitates, possibly thought to be carbides along the grain boundaries. Upon aging the sample at 1070°C/15min, the microstructure completely transforms to martensite. The tempering heat treatments (both with and without the prior aging) are similar to what was noticed in G91. The single step retains the microstructure similar to the as deposited one, while the sample with the prior aging looks like the sample aged at 1070°C, i.e. martensitic.

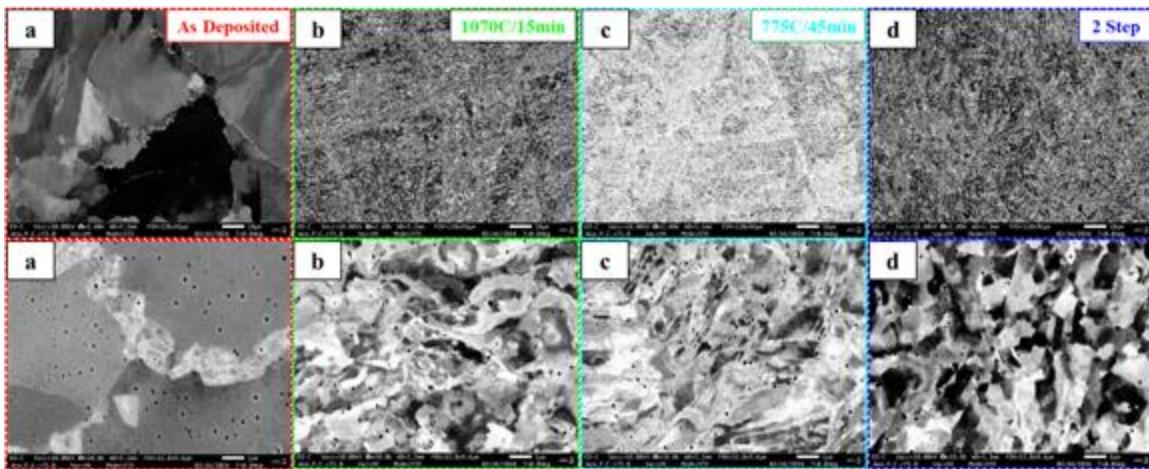


Figure 19: SEM of G92 alloy after heat treatments

4.3.2 Mechanical Behavior

As mentioned, the addition of W leads to an overall increase in the strength of these alloys. This is reflected in the room temperature tensile behavior, shown in Figure 20. The as deposited sample has UTS around 1100MPa with a strain to failure around 12%. Annealing the sample at 1070°C leads to a massive increase in the UTS to ~1500MPa. Similar to alloy G91, the tempering treatment leads to lower strengths, but improved ductilities. More work needs to be done in order to understand the mechanical behavior of this alloy and will be pursued in the upcoming FY25.

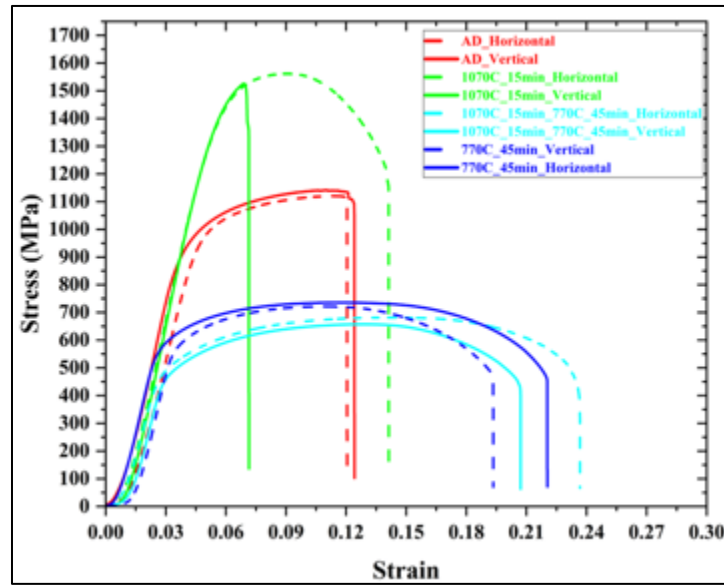


Figure 20: Room temperature mechanical behavior of the alloy G92 after different heat treatments

Conclusions and Future Work

5.1 Conclusions

The report continues on the work done in FY 2023 on the additive manufacturing of current materials on potential usage in nuclear applications. The following conclusions are drawn from the report.

1. Larger scale A709 alloys were successfully printed based on the study from previous year on optimizing the process parameters. The microstructural evolution of the alloy was studied after performing a series of heat treatments. The role of solution annealing the sample led to insights regarding the need for different heat treatments for additively manufactured alloys compared to their wrought counterparts. Precipitation treatment of this alloy, with and without prior solutionizing leads to forming a microstructure which contains different kinds of secondary and tertiary precipitates in the *fcc* matrix, which significantly enhance the mechanical behavior, as noted in room and elevated temperature tensile testing.
2. Similar observations were noted in printing of the ferritic martensitic steels, G91 and G92. A good combination of strength and ductility was obtained in both these alloys, in room temperature tensile testing, by a combination of different heat treatments.
3. This exercise proves that the additive manufacturing of the selected Fe-based current reactor materials, either austenitic stainless steel or ferritic/martensitic steels is very feasible, and more work needs to be done in order to understand the microstructure evolution during the depositions and also to further optimize the final microstructures.

5.2 Future Work

Based on the current results and discussions, there are still a few questions which need to be answered, and there is a scope to perform further characterization, for understanding both the microstructural evolution and mechanical behavior.

1. Large scale samples of optimized conditions need to be built for further mechanical testing including creep and creep fatigue.
2. Post-build treatment and thermal stability of the microstructures needs to be studied.
3. Furthermore, more analysis needs to be done to understand the microstructural evolution in F/M steels, i.e. G 91 and G 92.
4. Irradiation and corrosion testing, time permitting, will also need to be done on the AM samples and compared to their bulk counterparts.

Acknowledgements

This work was sponsored by the U.S. Department of Energy, under Contract No. DE-AC02-06CH11357 with Argonne National Laboratory, managed and operated by UChicago Argonne LLC. The authors acknowledge support for this work from the Advanced Materials and Manufacturing Technologies (AMMT) program. All the characterization work was performed at the Center for Nanoscale Materials, a U.S. Department of Energy Office of Science User Facility, was supported by the U.S. DOE, Office of Basic Energy Sciences, under Contract No. DE-AC02-06CH11357. Helpful discussions Drs. Meimei Li, Lin Gao, Isabella Van Rooyen, Peeyush Nandwana, and Subhashish Meher are gratefully acknowledged. We would also like to acknowledge Mark Messner for reviewing the report.

Chapter 7: References

- [1] W. J. Sames, F. A. List, S. Pannala, R. R. Dehoff, and S. S. Babu, “The metallurgy and processing science of metal additive manufacturing,” *International Materials Reviews*, vol. 61, no. 5, pp. 315–360, 2016, doi: 10.1080/09506608.2015.1116649.
- [2] C. Sun, Y. Wang, M. D. McMurtrey, N. D. Jerred, F. Liou, and J. Li, “Additive manufacturing for energy: A review,” *Appl Energy*, vol. 282, p. 116041, Jan. 2021, doi: 10.1016/J.APENERGY.2020.116041.
- [3] T. J. Maloy and S. Andrew, “Title: Laser Additive Manufacturing of F/M Steels for Radiation Tolerant Nuclear Components Intended for.”
- [4] Li and Meimei, “Advanced Materials and Manufacturing Technologies (AMMT) 2022 Roadmap.” [Online]. Available: www.anl.gov.
- [5] “Evaluation of LPBF Steels for Nuclear Applications Nuclear Science and Engineering Division.” [Online]. Available: www.anl.gov.
- [6] D. R. Harries, J. Standring, W. D. Barnes, and G. J. Lloyd, “U. K. FAST REACTOR MATERIALS PROGRAMME.,” *ASTM Special Technical Publication*, pp. 1197–1217, 1982, doi: 10.1520/STP34405S.
- [7] T.-L. Sham, Y. Wang, R. Bass, and X. Zhang, “A709 Qualification Plan Update and Mechanical Properties Data Assessment,” 2022. [Online]. Available: <http://www.art.inl.gov>
- [8] “Report on the Initial Loading of SS3 Specimens from the First Commercial Heat of Alloy 709 in Sodium Materials Test Loops for Long-term Exposure Applied Materials Division.” [Online]. Available: www.anl.gov.
- [9] Y. Wang, P. Hou, R. E. Bass, X. Zhang, and T.-L. Sham, “Interim Mechanical Properties Data from FY22 ORNL Testing of A709 with Precipitation Treatment for ASME Code Case Data Package,” 2022. [Online]. Available: www.osti.gov
- [10] R. L. Klueh and A. T. Nelson, “Ferritic/martensitic steels for next-generation reactors,” *Journal of Nuclear Materials*, vol. 371, no. 1–3, pp. 37–52, Sep. 2007, doi: 10.1016/j.jnucmat.2007.05.005.
- [11] “Designation: A213/A213M – 19a Standard Specification for Seamless Ferritic and Austenitic Alloy-Steel Boiler, Superheater, and Heat-Exchanger Tubes 1”, doi: 10.1520/A0213_A0213M-19A.

- [12] T. Hatakeyama, K. Sawada, M. Suzuki, and M. Watanabe, “Microstructure development of modified 9Cr-1Mo steel during laser powder bed fusion and heat treatment,” *Addit Manuf*, vol. 61, Jan. 2023, doi: 10.1016/j.addma.2022.103350.
- [13] L. Tan, W. Zhong, Y. Yang, K. G. Field, N. Sridharan, and A. T. Nelson, “Creep behavior of an additively manufactured 9Cr steel in the as-built condition,” *Journal of Nuclear Materials*, vol. 570, Nov. 2022, doi: 10.1016/j.jnucmat.2022.153943.
- [14] W. Zhong *et al.*, “Microstructures and mechanical properties of a modified 9Cr ferritic-martensitic steel in the as-built condition after additive manufacturing,” *Journal of Nuclear Materials*, vol. 545, Mar. 2021, doi: 10.1016/j.jnucmat.2020.152742.
- [15] J. Feng *et al.*, “Laser additive manufacturing and post-heat treatment on microstructure and mechanical properties of 9Cr steel,” *International Journal of Pressure Vessels and Piping*, vol. 198, Aug. 2022, doi: 10.1016/j.ijpvp.2022.104681.
- [16] B. P. Eftink *et al.*, “Tensile properties and microstructure of additively manufactured Grade 91 steel for nuclear applications,” *Journal of Nuclear Materials*, vol. 544, Feb. 2021, doi: 10.1016/j.jnucmat.2020.152723.
- [17] O. El-Atwani, B. P. Eftink, C. M. Cady, D. R. Coughlin, M. M. Schneider, and S. A. Maloy, “Enhanced mechanical properties of additive manufactured Grade 91 steel,” *Scr Mater*, vol. 199, Jul. 2021, doi: 10.1016/j.scriptamat.2021.113888.
- [18] F. Abe, “Precipitate design for creep strengthening of 9% Cr tempered martensitic steel for ultra-supercritical power plants,” *Sci Technol Adv Mater*, vol. 9, no. 1, p. 013002, Jan. 2008, doi: 10.1088/1468-6996/9/1/013002.
- [19] X. Zhou, C. Liu, L. Yu, Y. Liu, and H. Li, “Phase Transformation Behavior and Microstructural Control of High-Cr Martensitic/Ferritic Heat-resistant Steels for Power and Nuclear Plants: A Review,” *J Mater Sci Technol*, vol. 31, no. 3, pp. 235–242, Mar. 2015, doi: 10.1016/J.JMST.2014.12.001.
- [20] C. Cabet, F. Dalle, E. Gaganidze, J. Henry, and H. Tanigawa, “Ferritic-martensitic steels for fission and fusion applications,” *Journal of Nuclear Materials*, vol. 523, pp. 510–537, Sep. 2019, doi: 10.1016/J.JNUCMAT.2019.05.058.
- [21] P. Bajaj, A. Hariharan, A. Kini, P. Kürnsteiner, D. Raabe, and E. A. Jäggle, “Steels in additive manufacturing: A review of their microstructure and properties,” *Materials Science and Engineering: A*, vol. 772, Jan. 2020, doi: 10.1016/j.msea.2019.138633.

- [22] N. Haghdadi, M. Laleh, M. Moyle, and S. Primig, “Additive manufacturing of steels: a review of achievements and challenges,” Jan. 01, 2021, *Springer*. doi: 10.1007/s10853-020-05109-0.
- [23] T.-L. Sham, Y. Wang, R. Bass, and X. Zhang, “A709 Qualification Plan Update and Mechanical Properties Data Assessment,” 2022. [Online]. Available: <http://www.art.inl.gov>
- [24] Y. Wang, P. Hou, R. E. Bass, X. Zhang, and T.-L. Sham, “Interim Mechanical Properties Data from FY22 ORNL Testing of A709 with Precipitation Treatment for ASME Code Case Data Package,” 2022. [Online]. Available: www.osti.gov
- [25] R. Ding, J. Yan, H. Li, S. Yu, A. Rabiei, and P. Bowen, “Microstructural evolution of Alloy 709 during aging,” *Mater Charact*, vol. 154, pp. 400–423, Aug. 2019, doi: 10.1016/j.matchar.2019.06.018.
- [26] T. Sourmail and H. K. D. H. Bhadeshia, “Microstructural Evolution in Two Variants of NF709 at 1023 and 1073 K,” 2001.
- [27] J. Fan *et al.*, “Recovery of dislocation cell structures in 316L stainless steel manufactured by selective laser melting,” *Journal of Materials Research and Technology*, vol. 30, pp. 9472–9480, May 2024, doi: 10.1016/j.jmrt.2024.05.269.



Nuclear Science and Engineering Division

Argonne National Laboratory
9700 South Cass Avenue, Bldg. 212
Argonne, IL 60439

www.anl.gov



Argonne National Laboratory is a U.S. Department of Energy
laboratory managed by UChicago Argonne, LLC